hydrogen

MDPI

Article

Dispersion and Explosion Behavior of Hydrogen–Methane Mixtures in an Accident-Informed Multi-Compartment Apartment

Mi Jeong Lee [1], Sol Yi Lee [2], Min Seok Kim [2], Jong-Bae Baek [1] and Song-Su Tak [2,*]

[1] Department of Safety Engineering, Korea National University of Transportation, Chungju 27469, Republic of Korea; 652044@ut.ac.kr (M.J.L.); jbbaek@ut.ac.kr (J.-B.B.)
[2] Department of Hydrogen Safety Convergence, Far East University, Eumseong 27601, Republic of Korea; thftka0513@naver.com (S.Y.L.); rlaalstjryes@naver.com (M.S.K.)
* Correspondence: gogaek7727@gmail.com

Abstract

Hydrogen blending in residential gas networks requires assessment of gas transport across connected rooms and of explosion consequences if a flammable cloud forms. This study used FLACS-CFD to compare hydrogen blending ratios (HBRs) of 0, 5, 10, 15, and 20 vol%, the upper bound corresponding to the blend level demonstrated in distribution networks, in an accident-informed multi-compartment apartment. Two independent scenarios were evaluated: a 30 s release through a 6 mm opening at 0.025 barg and an explosion of a prescribed uniform cloud at an equivalence ratio of 1.05. Across 16 monitoring points, the maximum predicted fuel concentrations were 0.06575–0.07111 vol%, corresponding to 1.31–1.49% of the HBR-specific lower flammability limits. From HBR 0% to 20%, the maximum monitored concentration increased by 8.2%; the local maximum increased by 71.6% above the source but decreased by 16.3% outside the living room window. Under the independent explosion condition, maximum overpressure increased from 0.872 to 1.246 barg, maximum monitored pressure impulse increased by 21.3%, and the ignition-to-peak-pressure interval decreased by 12.7%. Analytical inventory estimates and comparisons with published data provided physical context for the calculated HBR-dependent trends, whereas the absolute values remain scenario-specific. By extending the comparison to connected apartment compartments, this study provides a numerical basis for selecting measurement locations and response metrics in future residential hydrogen-blending safety studies.

Keywords: hydrogen–methane mixture; hydrogen blending ratio; residential gas safety; gas leakage and dispersion; explosion overpressure; pressure impulse; FLACS-CFD

Check for updates

Academic Editors: Miroslav Variny and Isabel Cabrita

Received: 27 July 2026
Revised: 23 September 2026
Accepted: 28 September 2026
Published: 5 October 2026

Copyright: © 2026 by the authors. Licensee MDPI, Basel, Switzerland. This article is an open access article distributed under the terms and conditions of the Creative Commons Attribution (CC BY) license.

1. Introduction

Hydrogen is being considered as an energy carrier for reducing greenhouse gas emissions in energy uses that remain dependent on gaseous fuels [1]. Blending hydrogen into natural gas to produce hydrogen-blended natural gas (HBNG) provides a transitional option because existing gas networks can be used without the immediate construction of a dedicated hydrogen infrastructure [2,3]. Demonstration projects have supplied blends containing up to 20 vol% hydrogen through existing distribution networks and have examined network integrity, appliance operation, gas detection, and end user safety under project specific conditions [4]. The feasibility of hydrogen blending therefore depends not only on its potential carbon reduction benefit, but also on the compatibility and safety performance of the complete supply and end-use system. In Korea, a government program initiated in 2023 targeted safety verification across hydrogen-blended gas production, supply, and

use, including household appliances [5]. In Australia, Hydrogen Park South Australia supplies hydrogen blends through an existing network serving households, businesses, and schools [6]. These developments motivate the assessment of accidental releases in residential environments. Accordingly, HBRs up to 20 vol% were considered here, corresponding to the blend level demonstrated in distribution networks [4]; this range is not intended as a universal safety limit.

Hydrogen addition changes the physical and combustion properties of natural gas. Compared with methane, hydrogen has a lower molecular mass, higher diffusivity, wider flammability range, lower minimum ignition energy, and higher burning velocity [7,8]. These differences can affect the release rate, indoor transport, flammable cloud formation, flame acceleration, and pressure development rate of HBNG. The magnitude of these effects, however, depends on the HBR and on the release, enclosure, ventilation, and ignition conditions.

HBNG leakage and explosion behavior has also been examined in urban distribution networks, closed containers, utility tunnels, residential courtyards, and ship engine rooms [9–14], showing that the hazard depends strongly on the confinement and geometry of the space. Experiments in residential-scale enclosures have shown that methane–hydrogen accumulation depends on release and ventilation conditions and is spatially nonuniform [15,16]. Subsequent simulations examined kitchen leakage, ventilation in domestic houses, and confined spaces such as cupboards [17–19]. These studies identified source configuration, ventilation, and upper-region accumulation as important factors in residential dispersion.

Residential explosion studies have extended this work to the consequences of igniting hydrogen–methane clouds. Xu et al. [20] combined numerical simulations with experimental verification in a domestic kitchen. Pang et al. [21] compared leakage-generated nonuniform clouds with idealized uniform clouds, while Lv et al. [22] used leakage-generated concentration fields as the initial conditions for FLACS explosion calculations at HBRs of 0–20 vol%. Peng et al. [23] investigated flame propagation and pressure development in a residential building model. These studies show the importance of specifying how the combustible cloud is formed or prescribed when comparing explosion consequences.

Vented-enclosure experiments additionally demonstrate that explosion loading depends on both hydrogen fraction and enclosure conditions [24,25]. Lowesmith et al. [24] observed a relatively limited response at lower hydrogen fractions and a stronger increase at higher fractions; Torrado et al. [25] reported higher pressures for an 80:20 methane–hydrogen mixture than for methane in a domestic-scale vented chamber. Room layout and ignition location have also affected the computed pressure response in residential explosion studies [26,27]. This evidence motivates extending spatial comparisons beyond the source room to connected compartments and external openings.

High-resolution convection schemes provide another direction for numerical development. Deng [28] introduced the ROUND framework and the libROUNDSchemes library for OpenFOAM, with benchmark improvements in numerical dissipation and transported-structure preservation. The present work uses the built-in FLACS formulation; ROUND provides context for future comparisons of numerical approaches.

This study develops an accident-informed residential HBNG scenario based on the principal spatial layout and release circumstances of a selected apartment accident in Korea. The first stage examines HBNG release and dispersion under a low-pressure residential supply condition and evaluates concentration histories at 16 fixed monitoring points. The second stage compares maximum overpressure, pressure impulse, pressure development time, and temperature for HBRs of 0–20 vol% under a common near-stoichiometric fuel cloud condition. The objective is to compare how the predicted response to increasing HBR differs

between dispersion and conditional explosion and among the evaluated concentration, pressure, impulse, time, and temperature metrics. The study contributes a spatially resolved numerical comparison across connected apartment compartments to support the planning of subsequent residential safety investigations.

Table 1 summarizes the physical settings and principal variables investigated in earlier residential studies. The present work focuses on how the HBR response varies among the source region, inter-compartment transfer paths, and an exterior opening and how the conditional explosion response differs among pressure, impulse, timing, and temperature metrics.

Table 1. Comparison of previous residential HBNG dispersion and explosion studies with the present study.

Authors	Method and Geometry	Fuel Composition	Main Variables	Dispersion–Explosion Treatment
Lowesmith et al. [15]	Large scale experiment; ventilated residential room enclosure	CH_4 and CH_4–H_2 mixtures up to 50 vol% H_2	Release condition and ventilation	Dispersion only
Marangon and Carcassi [16]	Experiment; confined and ventilated enclosure	CH_4–H_2 mixtures	Ventilation and mixture composition	Dispersion only
Su et al. [17]	CFD; residential kitchen	HBRs up to 20 vol%	HBR, leakage rate, ventilation, and room dimensions	Dispersion only
Li et al. [18]	CFD; residential house and kitchen	HBNG mixtures	HBR and ventilation configuration	Dispersion and ventilation
Thawani et al. [19]	CFD; confined residential spaces and kitchen cupboards	Hydrogen and methane	Leakage diameter and source location	Dispersion only
Xu et al. [20]	CFD and experiment; residential kitchen	Natural gas and hydrogen–methane mixtures	Hydrogen content and ignition	Dispersion and explosion
Pang et al. [21]	CFD; residential kitchen	Multiple HBRs	HBR and gas cloud nonuniformity	Leakage generated and ideal uniform clouds compared
Lv et al. [22]	FLACS-CFD; residential kitchen	HBRs of 0–20 vol%	HBR	Leakage generated concentration field used for explosion
Peng et al. [23]	CFD; residential-building model	Multiple HBRs	HBR and explosion development	Prescribed explosion cases
Lowesmith et al. [24]	Experiment; vented enclosure	CH_4–H_2 mixtures	Hydrogen fraction and vented explosion	Premixed explosion
Torrado et al. [25]	Experiment; residential-scale vented chamber	CH_4 and 80:20 CH_4–H_2	Fuel composition	Premixed explosion
Yang, K., et al. [26] Yang, H., et al. [27]	CFD; residential kitchen and typical residence	Natural gas	Room layout and ignition location	Prescribed explosion cases
Present study	FLACS-CFD; accident informed multi-compartment apartment	CH_4–H_2 mixtures with HBRs of 0–20 vol%	HBR under fixed release and explosion conditions	Low pressure dispersion and conditional explosion evaluated independently

The apartment model includes a kitchen, living room, three bedrooms, boiler room, veranda, and connecting openings, with the layout and release mechanism informed by an accident in Korea. A time-limited dispersion scenario and a separately prescribed near-stoichiometric explosion cloud are used to examine transport and conditional consequences. This framework extends the spatial comparison to connected residential compartments and provides measurement locations and response quantities for subsequent apartment-scale investigations.

2. Materials and Methods

2.1. Accident-Informed Scenario Selection

To define a representative residential leakage scenario, an accident-informed approach was adopted based on an analysis of city gas accidents in Korea between 2014 and 2023 [29,30]. Among the 952 gas accidents recorded during this period, 183 involved city gas, and 56 were classified as indoor leakage accidents. Of the indoor leakage accidents, 50 resulted in fire or explosion, and 45 occurred in residential buildings [29].

Housing data indicated that multiunit housing accounted for 79.2% of the Korean housing stock and that apartments represented the largest proportion of multiunit dwellings. Housing units with a floor area of 60–100 m^2 formed the largest floor area category [29,31]. Based on these accident and housing characteristics, an approximately 100 m^2 multicompartment apartment was selected as the representative residential geometry.

The release mechanism was derived from an apartment accident in which a gas range had been removed without sealing the remaining gas hose. Gas was subsequently released indoors after the valve was opened and accumulated before ignition [29]. The numerical scenario represented gas discharge from an uncapped hose–fuse cock connection in the kitchen following gas range removal and valve opening. The accident record was used to define the residential setting, principal spatial layout, and release mechanism.

The numerical assessment consisted of two independent analysis stages. The first stage examined HBNG release and dispersion under a low-pressure residential supply condition and compared the predicted concentrations at 16 monitoring locations with the mixture-specific flammability limits and examined the spatial distributions. The second stage evaluated explosion consequences using a prescribed near-stoichiometric HBNG cloud and compared the effects of HBR on overpressure, pressure impulse, pressure development time, and temperature. The dispersion field was not used as the initial condition for the explosion simulations.

2.2. Apartment Geometry and Computational Model

2.2.1. Apartment Geometry

The model included a kitchen, living room, three bedrooms, boiler room, veranda, and the internal openings connecting these spaces. The external dimensions of the apartment were 10.2 m × 10.6 m × 2.4 m. The walls, floor, and ceiling were modeled with a thickness of 0.1 m, producing an internal airspace envelope of approximately 10.0 m × 10.4 m × 2.2 m. The resulting floor area corresponded to an approximately 100 m^2 class apartment. Figure 1 shows the apartment geometry, the leakage and ignition locations, the internal openings, and the monitoring points.

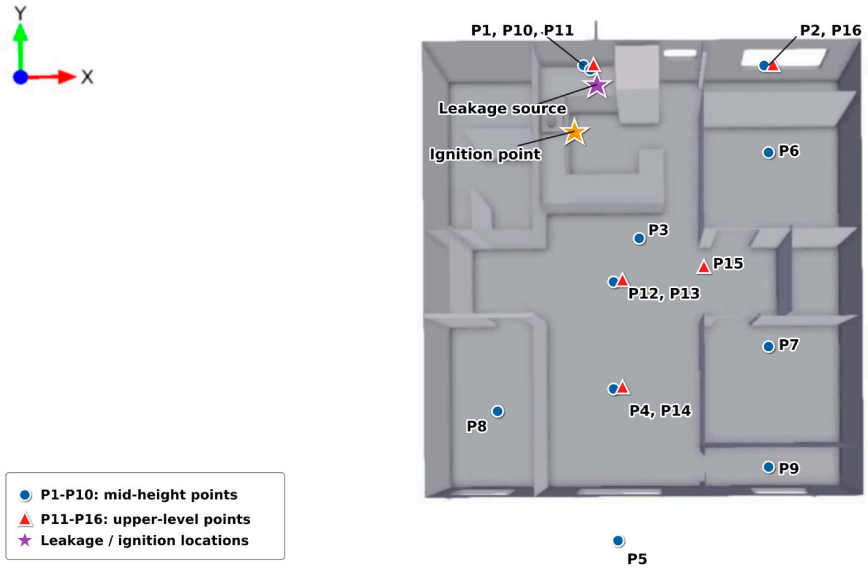

Figure 1. Apartment geometry used in the simulations, showing the principal indoor compartments, leakage and ignition locations, internal openings, and monitoring points P1–P16.

The kitchen and living room formed the principal open space. The bedrooms, boiler room, and veranda were connected to this area through internal openings and passage regions. The kitchen source was connected to the adjacent rooms through the kitchen–living room opening and upper inter-compartment pathways. This configuration allowed gas transport from the release location to the surrounding compartments and the spatial development of pressure and temperature during the explosion simulations to be evaluated.

The same apartment dimensions, internal partition arrangement, openings, and leakage source location were maintained for all HBR cases. The apartment geometry was embedded in a computational domain extending beyond the exterior boundaries to allow gas discharge and explosion venting through the modeled openings.

2.2.2. Governing Equations and Model Closure

The simulations were performed using FLACS-CFD version 25.2 (Gexcon AS, Bergen, Norway) [32]. FLACS-CFD was selected because its modelling framework combines compressible flow, gas dispersion, premixed deflagration, and the Porosity Distributed Resistance (PDR) approach for representing complex and partially unresolved geometrical features. Previous applications and validation studies have included hydrogen release, dispersion, and ignition scenarios [33,34].

Published experimental comparisons provide a basis for applying FLACS to hydrogen release and deflagration problems. Middha et al. [33] compared dispersion and subsequent explosion predictions with ignited impinging hydrogen jet experiments, while Hansen et al. [34] assessed flame propagation and pressure development against large-scale hydrogen explosion experiments in the FLAME facility. These studies informed the selection of the modelling framework used here. Case-specific benchmarking of the present release and explosion predictions against published data is presented in Section 4.2.

The model solves the Favre-averaged conservation equations for compressible flow and scalar transport on a structured Cartesian grid. The PDR formulation represents geometrical blockage through volume porosity and directional area porosities, with additional flow resistance from unresolved obstructions. Following the documented FLACS formu-

lation [34–37], the mass, momentum, enthalpy, fuel mass fraction, and mixture fraction equations are written as Equations (1)–(5). Repeated spatial indices imply summation.

$$\frac{\partial(\beta_v \rho)}{\partial t} + \frac{\partial\left(\beta_j \rho u_j\right)}{\partial x_j} = \frac{\dot{m}}{V} \tag{1}$$

$$\frac{\partial(\beta_v \rho u_i)}{\partial t} + \frac{\partial\left(\beta_j \rho u_i u_j\right)}{\partial x_j} = -\beta_v \frac{\partial p}{\partial x_i} + \frac{\partial\left(\beta_j \sigma_{ij}\right)}{\partial x_j} + F_{o,i} + F_{w,i} + \beta_v(\rho - \rho_0) g_i \tag{2}$$

$$\frac{\partial(\beta_v \rho h)}{\partial t} + \frac{\partial\left(\beta_j \rho u_j h\right)}{\partial x_j} = \frac{\partial}{\partial x_j}\left(\beta_j \frac{\mu_{\text{eff}}}{\sigma_h} \frac{\partial h}{\partial x_j}\right) + \beta_v \frac{Dp}{Dt} + \frac{\dot{Q}}{V} \tag{3}$$

$$\frac{\partial(\beta_v \rho Y_F)}{\partial t} + \frac{\partial\left(\beta_j \rho u_j Y_F\right)}{\partial x_j} = \frac{\partial}{\partial x_j}\left(\beta_j \frac{\mu_{\text{eff}}}{\sigma_F} \frac{\partial Y_F}{\partial x_j}\right) + R_F \tag{4}$$

$$\frac{\partial(\beta_v \rho \xi)}{\partial t} + \frac{\partial\left(\beta_j \rho u_j \xi\right)}{\partial x_j} = \frac{\partial}{\partial x_j}\left(\beta_j \frac{\mu_{\text{eff}}}{\sigma_\xi} \frac{\partial \xi}{\partial x_j}\right) \tag{5}$$

Here, β_v is the volume porosity, and β_j is the area porosity in direction j; ρ, u_i, p, and h denote density, velocity, pressure, and specific enthalpy, respectively. Y_F is the fuel mass fraction, and ξ is the mixture fraction. The terms $\dot{m}/V$ and $\dot{Q}/V$ represent volumetric mass and heat sources, σ_{ij} is the stress tensor, $F_{o,i}$ and $F_{w,i}$ are resistance forces associated with sub-grid obstructions and walls, and ρ_0 and g_i are the reference density and gravitational acceleration, respectively. The coefficient μ_{eff} is the effective viscosity, σ_h, σ_F, and σ_ξ are transport model coefficients, and R_F is the combustion source term. The dispersion stage uses these transport equations without combustion.

The K-EPS setting was applied for turbulence closure. Its two-equation k–ε formulation transports turbulent kinetic energy k and its dissipation rate ε, with an effective viscosity that includes molecular and turbulent contributions [34–37]. The documented transport and closure relations are given in Equations (6)–(9). This closure was used because it is integrated with the PDR representation of wall and unresolved-obstruction effects in the FLACS framework.

$$\frac{\partial(\beta_v \rho k)}{\partial t} + \frac{\partial\left(\beta_j \rho u_j k\right)}{\partial x_j} = \frac{\partial}{\partial x_j}\left(\beta_j \frac{\mu_{\text{eff}}}{\sigma_k} \frac{\partial k}{\partial x_j}\right) + \beta_v P_k - \beta_v \rho \varepsilon \tag{6}$$

$$\frac{\partial(\beta_v \rho \varepsilon)}{\partial t} + \frac{\partial\left(\beta_j \rho u_j \varepsilon\right)}{\partial x_j} = \frac{\partial}{\partial x_j}\left(\beta_j \frac{\mu_{\text{eff}}}{\sigma_\varepsilon} \frac{\partial \varepsilon}{\partial x_j}\right) + \beta_v P_\varepsilon - C_{2\varepsilon} \beta_v \rho \frac{\varepsilon^2}{k} \tag{7}$$

$$\mu_{\text{eff}} = \mu + \rho C_\mu \frac{k^2}{\varepsilon} \tag{8}$$

$$P_k = G_s + G_w + G_b + G_o, \qquad P_\varepsilon = C_{1\varepsilon} \frac{\varepsilon}{k} P_k \left(1 + C_{3\varepsilon} R_f\right) \tag{9}$$

In Equations (6)–(9), G_s, G_w, G_b, and G_o denote turbulence production associated with shear, walls, buoyancy, and sub-grid obstructions, respectively; and R_f represents the buoyancy correction in dissipation production. The documented constants are $C_\mu = 0.09$, $C_{1\varepsilon} = 1.44$, $C_{2\varepsilon} = 1.92$, and $C_{3\varepsilon} = 0.8$, with $\sigma_k = 1.0$ and $\sigma_\varepsilon = 1.3$ as documented in the FLACS-CFD version 25.2 user manual [37].

The BETA3 combustion model setting was applied to the conditional explosion simulations. The FLACS β-flame formulation represents premixed turbulent flame propagation using a numerically thickened reaction zone. The burning rate is governed by mixture-dependent laminar, quasi-laminar, and turbulent burning velocity correlations, together with sub-grid contributions from flame folding, turbulence, and unresolved obstructions [34–36]. BETA3 was selected as the FLACS premixed deflagration model appropriate for evaluating flame acceleration and pressure development in obstructed and compartmented geometries. The model does not explicitly resolve detailed chemical kinetics or the physical laminar flame thickness.

2.2.3. Numerical Discretization

The equations were discretized using the finite volume method on a structured Cartesian grid, with staggered velocity components and cell-centered scalar variables. The documented FLACS spatial scheme uses a second-order treatment of diffusion and a second-order κ scheme combining upwind and central difference contributions for convection, with limiters for selected equations [37]. Time integration used the first-order backward Euler formulation, with time-step control based on the applicable CFL and stability constraints. Pressure–velocity coupling used the SIMPLE pressure correction method extended to compressible flow [34–37]. Three-dimensional output intervals were 1.0 s for dispersion and 0.005 s for explosion; monitoring histories were recorded at solver time-step resolution.

2.2.4. Computational Grids

Analysis-specific grids were applied to the dispersion and explosion simulations. In the dispersion simulations, local refinement was introduced around the 6 mm release source to resolve the near-source jet and concentration gradients. The resulting dispersion grids contained 263,520–302,940 control volumes. The same computational domain, apartment geometry, leakage location, and 16 monitoring locations were maintained for the five HBR cases. The difference in the number of control volumes arose from the local refinement and grid-spacing adjustment around the release source; the computational domain, the grid outside the refined source region, and the monitoring locations were identical for all HBR cases.

The explosion simulations employed a common computational domain of 14.25 m × 22.25 m × 10.0 m. The grid consisted of 28 × 41 × 20 control volumes, corresponding to 22,960 cells. The same computational domain, grid arrangement, apartment geometry, and porosity field were used for all explosion cases. Only the prescribed CH_4–H_2 composition was varied according to the HBR, allowing the explosion responses to be compared under common geometric and numerical conditions. The resulting cell size was approximately 0.5 m, resolving the 2.2 m indoor height with four to five cells.

2.3. Monitoring and Output Configuration

Sixteen fixed monitoring points were placed throughout the accident-informed apartment model to characterize the spatial and temporal transport of the released HBNG. The monitoring locations covered the kitchen, living room, boiler room, three bedrooms, veranda, an exterior location outside the living room window, the region near the leakage source, and the upper parts of the principal gas transfer pathways.

P1–P9 were positioned in the principal rooms and the exterior region to evaluate room level gas migration. P10 was located near the leakage source. P11 and P13–P16 were placed at ceiling level or within upper connecting regions to examine vertical transport and gas movement between compartments, While P12 was positioned at mid-height at the kitchen-living room connection. The coordinates of all 16 points were maintained consistently across the five dispersion cases so that the effects of HBR could be compared at the same physical locations. The monitoring point coordinates are presented in Table 2.

Table 2. Monitoring locations used in the dispersion simulation.

Point	Location	Coordinates (x, y, z), m
P1	Kitchen	(3.70, 10.00, 1.30)
P2	Boiler room	(8.00, 10.00, 1.30)
P3	Front of kitchen island	(5.00, 6.00, 1.30)
P4	Living room	(4.50, 2.50, 1.30)
P5	Outside the living room window	(4.50, −1.00, 1.30)
P6	Bedroom 1	(8.00, 8.00, 1.30)
P7	Bedroom 2	(8.00, 3.50, 1.30)
P8	Bedroom 3	(1.70, 2.00, 1.30)
P9	Veranda	(8.00, 0.70, 1.30)
P10	Near leakage point	(3.85, 10.00, 1.30)
P11	Ceiling above leakage source	(3.93, 10.00, 2.05)
P12	Mid-height point at kitchen–living room connection	(4.50, 5.00, 1.50)
P13	Upper point at kitchen living room connection	(4.50, 5.00, 2.05)
P14	Living room ceiling	(4.50, 2.50, 2.05)
P15	Upper branching pathway	(6.50, 5.30, 2.05)
P16	Upper boiler room	(8.00, 10.00, 2.05)

The primary dispersion variable was MoleFractionFuel, which represents the total concentration of the blended CH_4–H_2 fuel rather than the concentration of either component separately. Time histories were obtained at P1–P16. For each HBR, the largest value recorded among these 16 points is reported as the maximum monitored concentration. Three-dimensional concentration fields and vertical and horizontal cut planes were also extracted at selected times to examine transport of the released fuel through the apartment.

For the conditional explosion simulations, the principal output variables were instantaneous pressure (Pressure), maximum pressure attained during the simulation (PressureMax), pressure impulse (PressureImpulse), and temperature (Temperature). Three-dimensional fields and planar sections were used as the primary basis for comparing the spatial pressure and temperature responses among the HBR cases. Local time histories at selected monitoring locations were used to support the analysis, including the common near-source location used to compare the maximum temperature response. Explosion output data were recorded at intervals of 0.005 s. The variables and units used in the analysis are summarized in Table 3. Explosion monitoring used the same 16 points (P1–P16) listed in Table 2; the near-source temperature was evaluated at P10, and the maximum monitored pressure impulse occurred at P7 (Bedroom 2) for HBR 0% and at P6 (Bedroom 1) for HBRs of 5–20%.

Table 3. Principal output variables and units.

Analysis Stage	Output Quantity	Description	Unit
Dispersion	MoleFractionFuel	Total volumetric fraction of the blended fuel	m^3/m^3
Explosion	Pressure	Instantaneous gauge pressure	barg
Explosion	PressureMax	Maximum gauge pressure attained during the simulation	barg
Explosion	Pressure impulse	Time-integrated pressure load	Pa·s
Explosion	Temperature	Gas temperature	K

2.4. Leakage and Dispersion Conditions

Five binary CH_4–H_2 mixtures with HBRs of 0, 5, 10, 15, and 20 vol% were considered. Because the composition of supplied natural gas can vary with source and supply conditions, methane was adopted as the reference natural gas component to isolate the effect of hydrogen addition under controlled fuel composition conditions. HBR was defined as the volumetric fraction of hydrogen in the total fuel mixture. The corresponding CH_4 and H_2 compositions and the lower and upper flammability limits are presented in Table 4. The HBR-specific flammability limits were adopted from the previous analysis of indoor city gas leakage scenarios [29].

Table 4. Fuel compositions, flammability limits, and calculated release characteristics.

HBR (Vol%)	CH_4 (Vol%)	H_2 (Vol%)	LFL (Vol%)	UFL (Vol%)	Mass Flow Rate (g/s)	Release Velocity (m/s)
0	100	0	5.00	15.00	1.383	86.083
5	95	5	4.93	15.62	1.352	87.744
10	90	10	4.87	16.30	1.321	89.819
15	85	15	4.81	17.04	1.289	92.049
20	80	20	4.76	17.85	1.256	94.454

LFL and UFL values were adopted from Ref. [29]. The natural gas component was represented by pure methane.

The leakage source was located in the kitchen at coordinates (4.0, 9.6, 1.3) m and directed along the negative *y*-axis. The source represented gas discharged from an uncapped hose–fuse cock connection after removal of the gas range. The leakage location and direction were determined from the accident scenario described in Section 2.1. The release opening had a diameter of 6 mm, corresponding to the internal diameter of the residential gas hose remaining after removal of the gas range.

The upstream gas was specified at a gauge pressure of 0.025 barg (2.5 kPa) and a temperature of 293.15 K. The pressure represented a low-pressure city gas supply condition consistent with the operating pressure range addressed in KGS FU551 [38]. The release source was generated using the hole size method in the FLACS Leak Wizard, with a discharge coefficient of 0.85 and the Ewan–Moodie pseudo-source model [39]. From the supply conditions, opening diameter, discharge coefficient, and fuel composition, the wizard calculates the mass flow rate, velocity, area, and thermodynamic state of the pseudo-source jet. Because mixture density decreases as HBR increases, the calculated mass flow generally decreased while jet velocity increased at the fixed pressure and opening, as shown in Table 4.

Dedicated provisions for the installation and response performance of HBNG detectors in general residential rooms have not yet been established in the KGS codes reviewed for this study. The release duration was therefore defined by referring to detector performance criteria applicable to other gas facilities. KGS FU551 specifies that gas leak alarms installed in city gas regulator rooms should activate within 60 s at a preset concentration not exceeding 25% of the lower flammability limit [38]. KGS FU211 Clause 2.8.2.1.4 specifies that the time from gas detection to alarm transmission should generally be within 30 s at a concentration corresponding to 1.6 times the alarm set point [40]. The same 30 s performance criterion is provided in KOSHA GUIDE P-166 for gas leak detection and alarm systems [41]. Based on these criteria, a 30 s release period was prescribed as a code-referenced comparison window. It provides a bounded release duration for comparing the HBR cases and is not intended to represent detector-initiated isolation (Section 4.2.1).

The dispersion simulations represented a quiescent indoor environment at an ambient temperature of 293.15 K and a pressure of 101,325 Pa. The initial turbulence field was defined using a characteristic velocity of 1.0 m/s, a relative turbulence intensity of 0.05, and a turbulence length scale of 0.05 m. In FLACS-CFD, these inputs determine the initial turbulent kinetic energy and turbulent dissipation rate and were applied consistently across all HBR cases. The ground roughness and reference height were set to 0.002 and 10 m, respectively. No mechanically imposed background airflow or Pasquill atmospheric stability class was applied. The six external boundaries of the computational domain were assigned the NOZZLE condition following the FLACS guidance for dispersion simulations [42]. All exterior windows and internal doors were modeled as open in both the dispersion and the explosion simulations.

Each dispersion simulation was conducted for 60 s. The source remained active for the first 30 s, followed by a 30 s post-release period during which continued transport and dilution were evaluated. The dispersion analysis included concentration time histories at P1–P16 and three-dimensional and planar concentration distributions. Across the dispersion simulations, the leakage location, opening diameter, supply pressure, release duration, ambient conditions, apartment geometry, and ventilation state were held constant. The mass flow rate and release velocity varied with fuel composition, as reported in Table 4. The leakage and dispersion simulation conditions are summarized in Table 5.

Table 5. Leakage and dispersion simulation conditions.

Parameter	Condition
Leakage location	(4.0, 9.6, 1.3) m
Leakage direction	Negative y-direction
Opening diameter	0.006 m (6 mm)
Supply pressure	0.025 barg (2.5 kPa)
Gas temperature	293.15 K
Release rate calculation	Hole size based
Discharge coefficient	0.85
Pseudo-source model	Ewan–Moodie
Release type	Steady-state point jet
Release duration	30 s
Ambient temperature	293.15 K
Ambient pressure	101,325 Pa
Indoor airflow condition	Quiescent
Characteristic velocity for turbulence initialization	1.0 m/s
Relative turbulence intensity	0.05
Turbulence length scale	0.05 m
Ground roughness	0.002 m
Reference height	10 m
External boundary condition	NOZZLE on all six boundaries
Total simulation time	60 s

2.5. Explosion Simulation

To evaluate how HBR influences explosion consequences when a flammable mixture is present, five explosion cases were established under common geometric and initial conditions. A uniform HBNG cloud was assigned to the indoor air space of the apartment. The fuel region originated at (0.1, 0.1, 0.1) m and had dimensions of 10.0 m × 10.4 m × 2.2 m, corresponding to the modeled indoor airspace envelope.

The CH_4–H_2 composition of the fuel cloud was varied according to the five HBR conditions presented in Table 4. An equivalence ratio of 1.05 was applied to all cases to represent

a common near-stoichiometric condition. The same fuel region, equivalence ratio, ambient conditions, ignition setting, apartment geometry, computational grid, and porosity field were maintained across all explosion simulations. Only the prescribed CH_4–H_2 composition was varied, allowing the effects of HBR on the magnitude and temporal development of the pressure and temperature responses to be compared under consistent conditions.

Point ignition was applied at coordinates (3.5, 8.5, 1.7) m at 0.1 s. The ignition duration was set to 0 s. The initial temperature and pressure were 293.15 K and 101,325 Pa, respectively. The six external boundaries of the computational domain were assigned the EULER boundary condition.

The explosion simulations used the common computational domain and grid described in Section 2.2. The end time was determined automatically by FLACS-CFD using the TMAX = −1 setting. The pressure and temperature responses were evaluated using the output variables described in Section 2.3, including three-dimensional distributions, planar sections, and selected monitoring point histories. The global maximum pressure and its occurrence time were used to compare the explosion pressure response among the HBR cases. The explosion simulation conditions are summarized in Table 6.

Table 6. Explosion simulation conditions.

Parameter	Condition
Fuel cloud location	Origin at (0.1, 0.1, 0.1) m
Fuel cloud dimensions	10.0 m × 10.4 m × 2.2 m
Fuel cloud distribution	Uniform
Fuel composition	CH_4–H_2 according to HBR
HBR	0, 5, 10, 15, and 20 vol%
Equivalence ratio	1.05
Ignition type	Point ignition
Ignition location	(3.5, 8.5, 1.7) m
Ignition time	0.1 s
Ignition duration	0 s
Initial temperature	293.15 K
Initial pressure	101,325 Pa
External boundary condition	EULER on all six boundaries
Computational domain	14.25 m × 22.25 m × 10.0 m

3. Results

3.1. Fuel Concentration and Flammability Assessment

The maximum monitored fuel concentration generally increased with HBR. The largest values among P1–P16 were 0.0006575 at HBR 0% and 0.0007111 at HBR 20%, corresponding to 0.06575 and 0.07111 vol%, respectively. The HBR 20% value was approximately 8.2% higher than the HBR 0% value.

Despite this increase, the monitored concentrations remained substantially below the HBR-specific lower flammability limits. The maximum monitored concentration represented 1.315% of the LFL at HBR 0% and 1.494% at HBR 20%. Across the five cases, the maximum monitored concentration reached only 1.31–1.49% of the corresponding LFL. Thus, the computed concentrations at P1–P16 remained below the adopted LFLs for the prescribed release. The equivalent stoichiometric cloud volume (Q9) also remained zero throughout the 60 s simulation for all HBRs. The maximum monitored concentrations and the corresponding HBR-specific lower flammability limits are summarized in Table 7.

Table 7. Maximum monitored fuel concentration and HBR-specific lower flammability limit.

HBR (Vol%)	Maximum MoleFractionFuel (m^3/m^3)	Time of Maximum (s)	LFL (Vol%)
0	0.0006575	31.10	5.00
5	0.0006780	32.48	4.93
10	0.0006890	31.29	4.87
15	0.0007027	32.21	4.81
20	0.0007111	37.20	4.76

The maximum monitored concentrations occurred between 31.10 and 37.20 s. In all cases, the monitored peak occurred after the release ended at 30 s, showing that fuel transport and redistribution continued for a short period following termination of the source. The near-constant ratio of the maximum monitored concentration to the volume-averaged released inventory is discussed in Section 4.2.1.

Figure 2 compares the maximum monitored fuel concentration and the percentage of the corresponding LFL for each HBR. Although both metrics generally increased with HBR, the LFL-normalized concentrations remained below 1.5% in all cases.

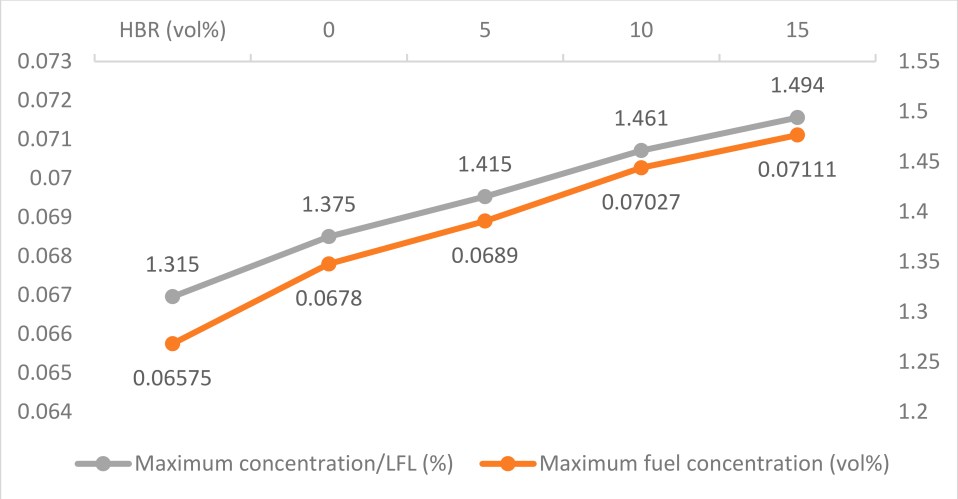

Figure 2. Maximum monitored fuel concentration and its relationship to the HBR-specific lower flammability limit.

3.2. Spatial Distribution and Temporal Variation of Released HBNG

The concentration distributions at the end of the 30 s release period showed that the HBNG cloud developed primarily from the kitchen source toward the kitchen–living room connection and adjacent indoor spaces. Figure 3 presents the MoleFractionFuel distributions for the five HBR cases using a common concentration range of 0–0.0008 m^3/m^3. The overall transport pattern was similar among the cases, while the extent and local concentration of the fuel cloud varied with HBR.

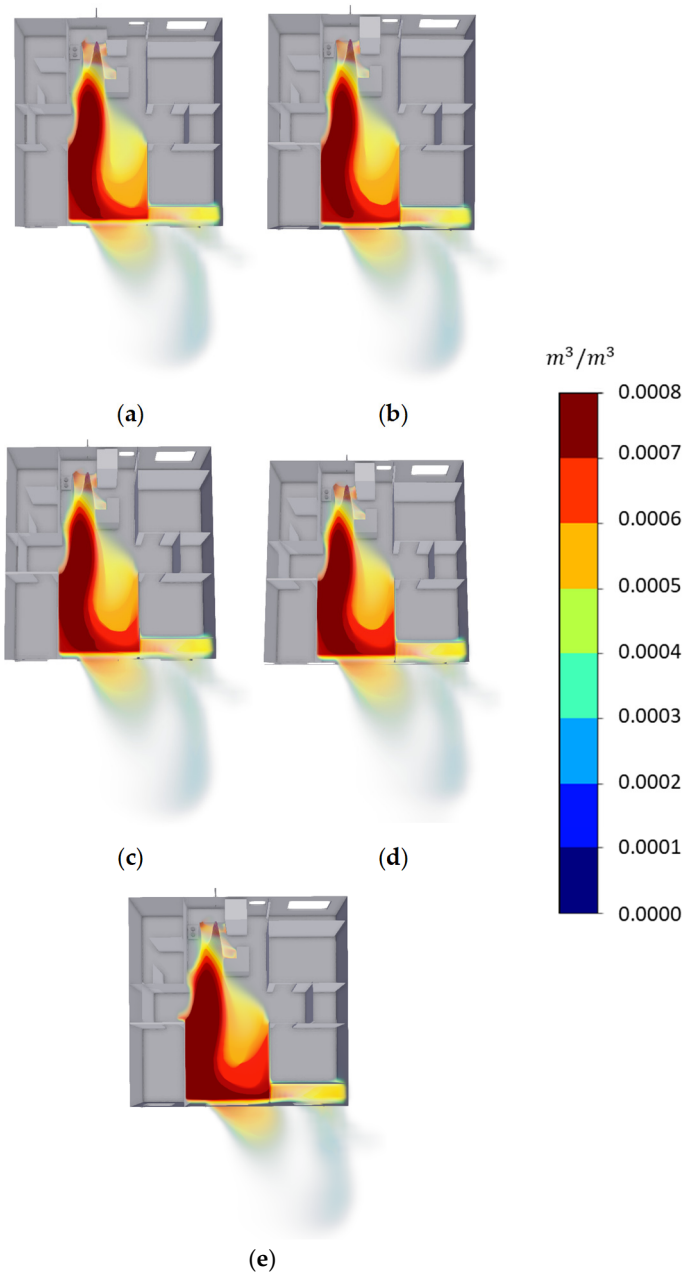

Figure 3. Three-dimensional MoleFractionFuel distributions at t = 30 s for HBRs of 0, 5, 10, 15, and 20 vol%. A common concentration range of 0–0.0008 m^3/m^3 was applied to all panels. (**a**) HBR 0 vol%, (**b**) HBR 5 vol%, (**c**) HBR 10 vol%, (**d**) HBR 15 vol%, (**e**) HBR 20 vol%.

The vertical section at x ≈ 3.84 m showed the upward transport of the released fuel near the leakage source and its distribution toward the upper part of the kitchen. The horizontal section at z ≈ 2.17 m showed the movement of the fuel through the upper kitchen–living room pathway and the connected spaces. The differences between HBR 0% and 20% were more apparent in selected upper level regions than in the overall cloud shape, as shown in Figure 4.

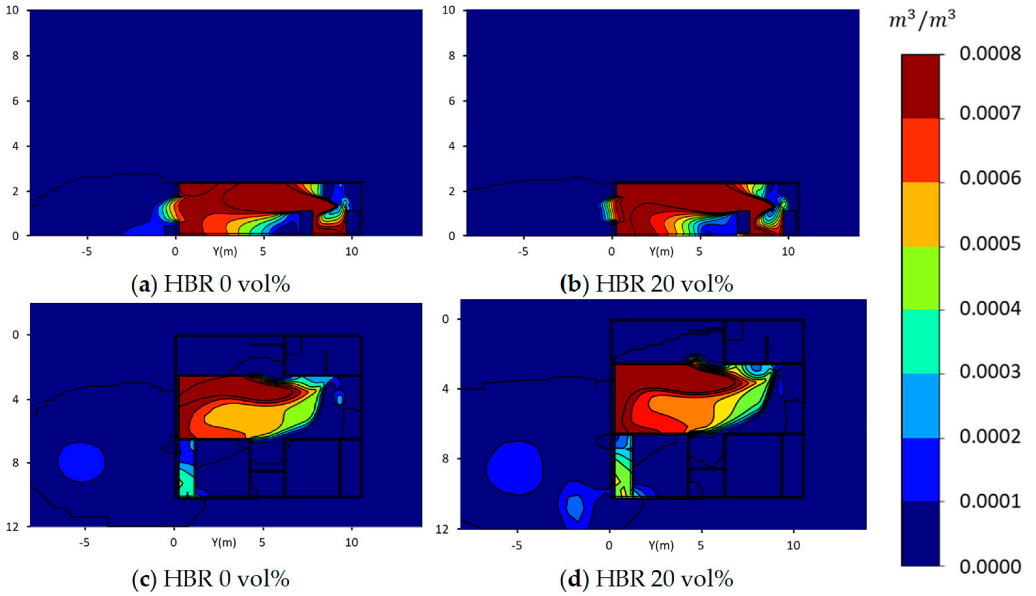

Figure 4. Comparison of the concentration distributions for HBR 0% and 20%: (**a**,**b**) vertical sections at x ≈ 3.84 m and (**c**,**d**) horizontal sections at z ≈ 2.17 m. A common concentration scale was applied to all panels.

The location-specific maximum concentrations did not change uniformly with HBR. As summarized in Table 8 and Figure 5, the maximum value recorded at P11 during the 60 s simulation increased from 0.02152 vol% at HBR 0% to 0.03694 vol% at HBR 20%, corresponding to an increase of 71.6%. The maximum at P15 in the upper branching passage increased by 16.3%, while that at P3 in front of the kitchen island increased by 19.0%. At P14 on the living room ceiling, the maximum increased from 0.06313 to 0.07111 vol% (12.6%).

Table 8. Selected location-specific maximum fuel concentration for HBR 0% and 20%.

Point	Location	HBR 0% (Vol%)	HBR 20% (Vol%)	Change (%)
P3	Front of kitchen island	0.03655	0.04348	19.0
P5	Outside the living room window	0.03582	0.02997	−16.3
P11	Ceiling above leakage source	0.02152	0.03694	71.6
P12	Mid-height point at kitchen–living room	0.06575	0.06728	2.3
P14	Living room ceiling	0.06313	0.07111	12.6
P15	Upper branching pathway	0.02303	0.02679	16.3

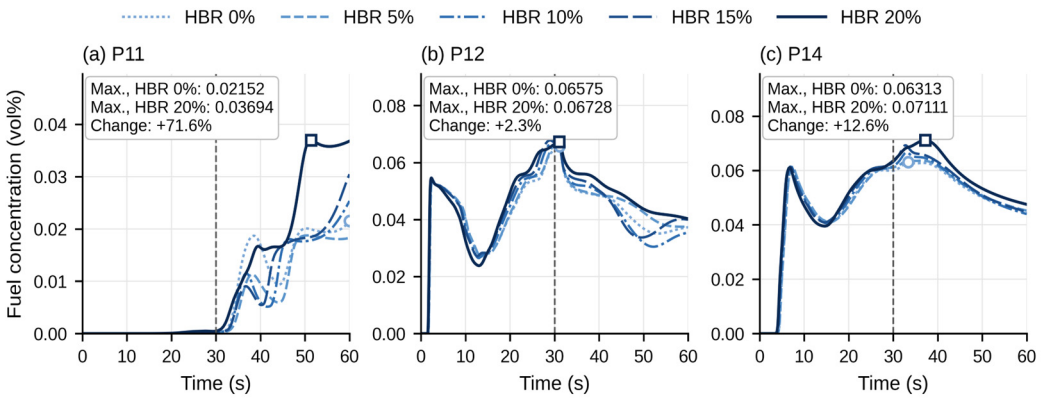

Figure 5. Time histories of MoleFractionFuel at selected upper-level and transfer path monitoring points: (**a**) P11, (**b**) P12, and (**c**) P14. The vertical dashed line indicates the end of the release at t = 30 s. Annotated values indicate the maximum concentrations recorded during the 60 s simulation for HBR 0% and 20% and their relative changes; open markers indicate the times at which these maxima occurred.

At P12, located at the mid-height kitchen–living room connection, the maximum concentration increased slightly from 0.06575 to 0.06728 vol% (2.3%). In contrast, the maximum outside the living room window at P5 decreased from 0.03582 to 0.02997 vol% (−16.3%). These results show that increasing HBR did not produce a uniform concentration response at all locations.

At P11, the maximum concentration increased from 0.02152 to 0.03694 vol%, equivalent to an absolute increase of 0.01542 percentage points. Both values remained well below the corresponding LFLs. Thus, the relatively large percentage increase at this location occurred within a low concentration range.

Figure 5 presents the concentration histories at P11, P12, and P14 for all HBR cases. The vertical dashed line marks termination of the release at 30 s, and the annotations report the HBR 0% and 20% peak values and their relative changes. MoleFractionFuel represents the total CH_4–H_2 fuel mixture; therefore, the observed upper-level patterns indicate transport of the blended fuel rather than independent hydrogen segregation. The physical basis of this redistribution is examined in Section 4.2.2.

3.3. Explosion Overpressure and Pressure Impulse Characteristics

Under the common near-stoichiometric fuel cloud and ignition conditions, the global maximum overpressure increased monotonically with HBR. As shown in Table 9, the maximum overpressure was 0.872 barg at HBR 0% and increased to 0.947, 1.043, 1.142, and 1.246 barg at HBRs of 5, 10, 15, and 20%, respectively. The HBR 20% case therefore produced a 42.9% higher maximum overpressure than the HBR 0% case.

Table 9. Maximum overpressure and its occurrence time under the explosion conditions.

HBR (Vol%)	Maximum Overpressure (barg)	Time of Maximum (s)	Elapsed Time After Ignition (s)	Increase Relative to HBR 0% (%)
0	0.872	0.3338	0.2338	-
5	0.947	0.3331	0.2331	8.6
10	1.043	0.3233	0.2233	19.6
15	1.142	0.3127	0.2127	31.0
20	1.246	0.3041	0.2041	42.9

The maximum pressure impulse among the monitoring points also increased continuously with HBR. The maximum monitored value increased from 4812.8 Pa·s at HBR 0% to 5034.4, 5311.4, 5577.3, and 5836.1 Pa·s at HBRs of 5, 10, 15, and 20%, respectively. The HBR 20% case therefore produced a 21.3% higher maximum monitored pressure impulse than the HBR 0% case. The relative increase in pressure impulse was smaller than the 42.9% increase in domain-wide maximum overpressure; this difference is examined in Section 4.2.3. The maximum monitored pressure impulse for each HBR is summarized in Table 10.

Table 10. Maximum monitored pressure impulse under the explosion conditions.

HBR (Vol%)	Maximum Monitored Pressure Impulse (Pa·s)	Increase Relative to HBR 0%
0	4812.8	-
5	5034.4	4.6%
10	5311.4	10.4%
15	5577.3	15.9%
20	5836.1	21.3%

The time at which the global maximum overpressure occurred decreased as HBR increased. The maximum occurred at 0.3338 s for HBR 0% and at 0.3041 s for HBR 20%. Because ignition was applied at 0.1 s, the elapsed time from ignition to the maximum overpressure decreased from 0.2338 to 0.2041 s, corresponding to a reduction of approximately 12.7%.

The simultaneous increase in maximum overpressure and decrease in the time required to reach the maximum indicate that the pressure response became stronger and developed more rapidly as the hydrogen fraction increased. The increase was continuous across the investigated HBR range, with no reversal in the global maximum pressure trend.

These results represent the HBR-dependent explosion response under the common fuel cloud condition defined in Section 2.5. The global maximum values were used as the principal comparison because they account for the highest pressure attained anywhere within the computational domain.

3.4. Spatial Distribution of Pressure and Temperature

Figure 6 presents the instantaneous pressure distributions on the Y–Z plane at 0.3 s for each HBR, and Figure 7 presents the corresponding PressureMax distributions on the X–Y plane. The pressure response was not confined to the vicinity of the ignition point, but propagated throughout the connected indoor spaces. Spatial differences appeared among the compartments because of the internal walls and openings, and pressure was also discharged outside through the external openings. This indicates that the pressure generated in the ignition region rapidly propagated through the apartment and affected areas away from the ignition point.

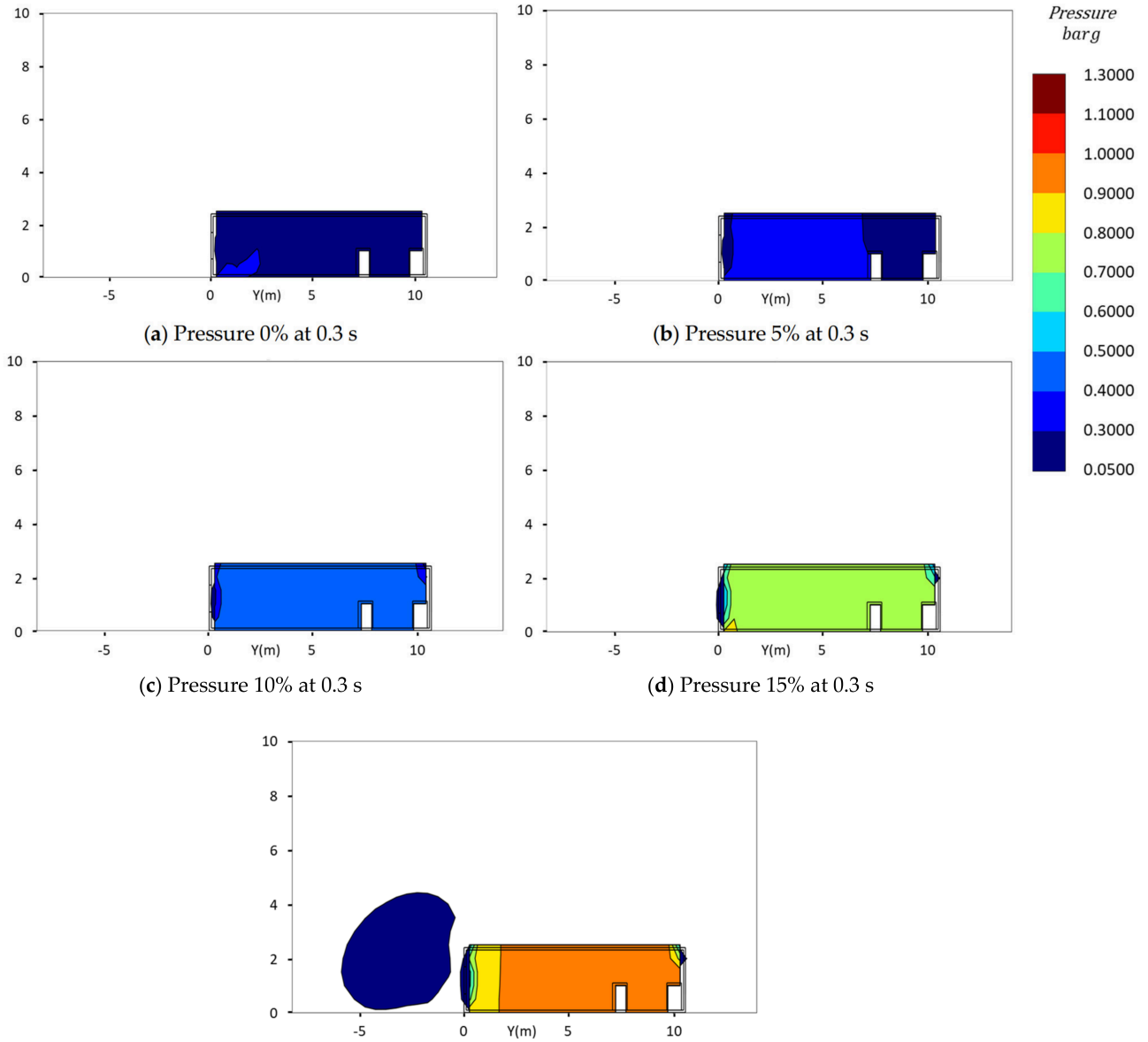

(**a**) Pressure 0% at 0.3 s (**b**) Pressure 5% at 0.3 s

(**c**) Pressure 10% at 0.3 s (**d**) Pressure 15% at 0.3 s

(**e**) Pressure 20% at 0.3 s

Figure 6. Spatial distributions of instantaneous pressure on the Y–Z plane at X ≈ 3.5 m at approximately 0.3 s for HBRs of (**a**) 0, (**b**) 5, (**c**) 10, (**d**) 15, and (**e**) 20 vol%. Pressure is given in barg.

The instantaneous pressure distribution at 0.3 s (Figure 6) did not increase consistently with HBR because the common snapshot represented different stages of calculated pressure development. The domain-wide maximum pressure occurred at 0.3338 s for HBR 0% and progressively earlier with increasing HBR, reaching 0.3041 s for HBR 20%. Figure 7e shows the maximum pressure attained at each location up to 0.3 s for HBR 20%. At that time, the HBR 20% case was closer to its global pressure peak than the HBR 0% case. The pressure maps should therefore be interpreted together with the timing results in Table 9.

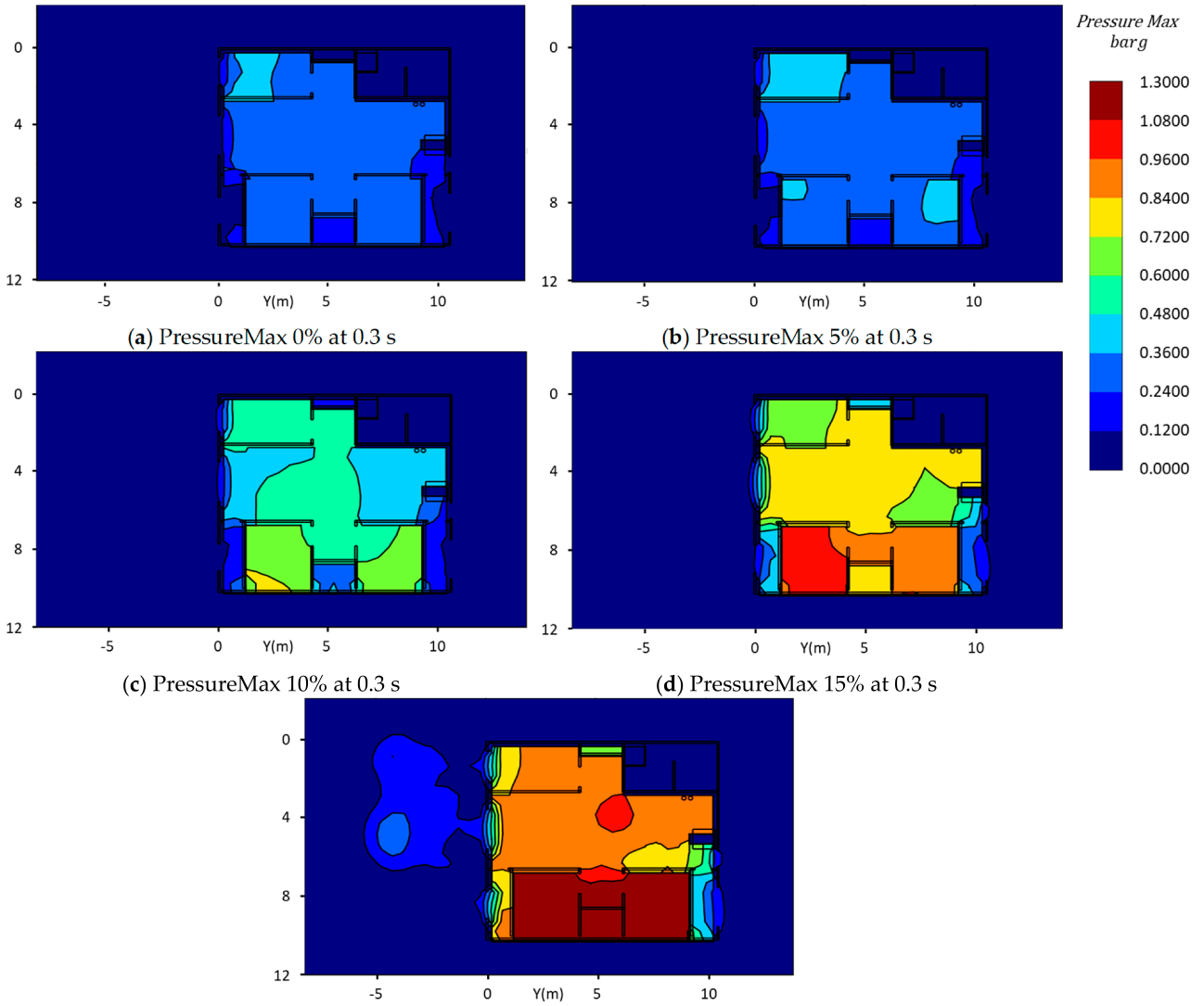

(**a**) PressureMax 0% at 0.3 s

(**b**) PressureMax 5% at 0.3 s

(**c**) PressureMax 10% at 0.3 s

(**d**) PressureMax 15% at 0.3 s

(**e**) PressureMax 20% at 0.3 s

Figure 7. Spatial distributions of PressureMax on the X–Y plane at Z = 1.25 m at approximately 0.3 s for HBRs of (**a**) 0, (**b**) 5, (**c**) 10, (**d**) 15, and (**e**) 20 vol%. PressureMax is given in barg.

PressureMax accumulated up to the displayed time (Figure 7) was not uniformly distributed throughout the apartment. Relatively high-pressure regions developed within the connected indoor compartments, whereas lower pressure ranges were observed outside the apartment after pressure was discharged through the external openings. As HBR increased, the indoor area corresponding to higher PressureMax ranges generally expanded. This spatial pattern was consistent with the increase in the domain-wide maximum overpressure from 0.872 barg at HBR 0% to 1.246 barg at HBR 20%.

Figure 8 presents the temperature distributions at 0.3 s using a common range of 293–2500 K. In all HBR cases, high-temperature combustion products occupied most of the connected indoor fuel region. The temperature distributions followed the internal compartment geometry and openings, and the high-temperature region extended from the vicinity of the ignition point into the connected indoor spaces. High-temperature combustion products were also discharged through the external openings, producing high-temperature regions outside the apartment.

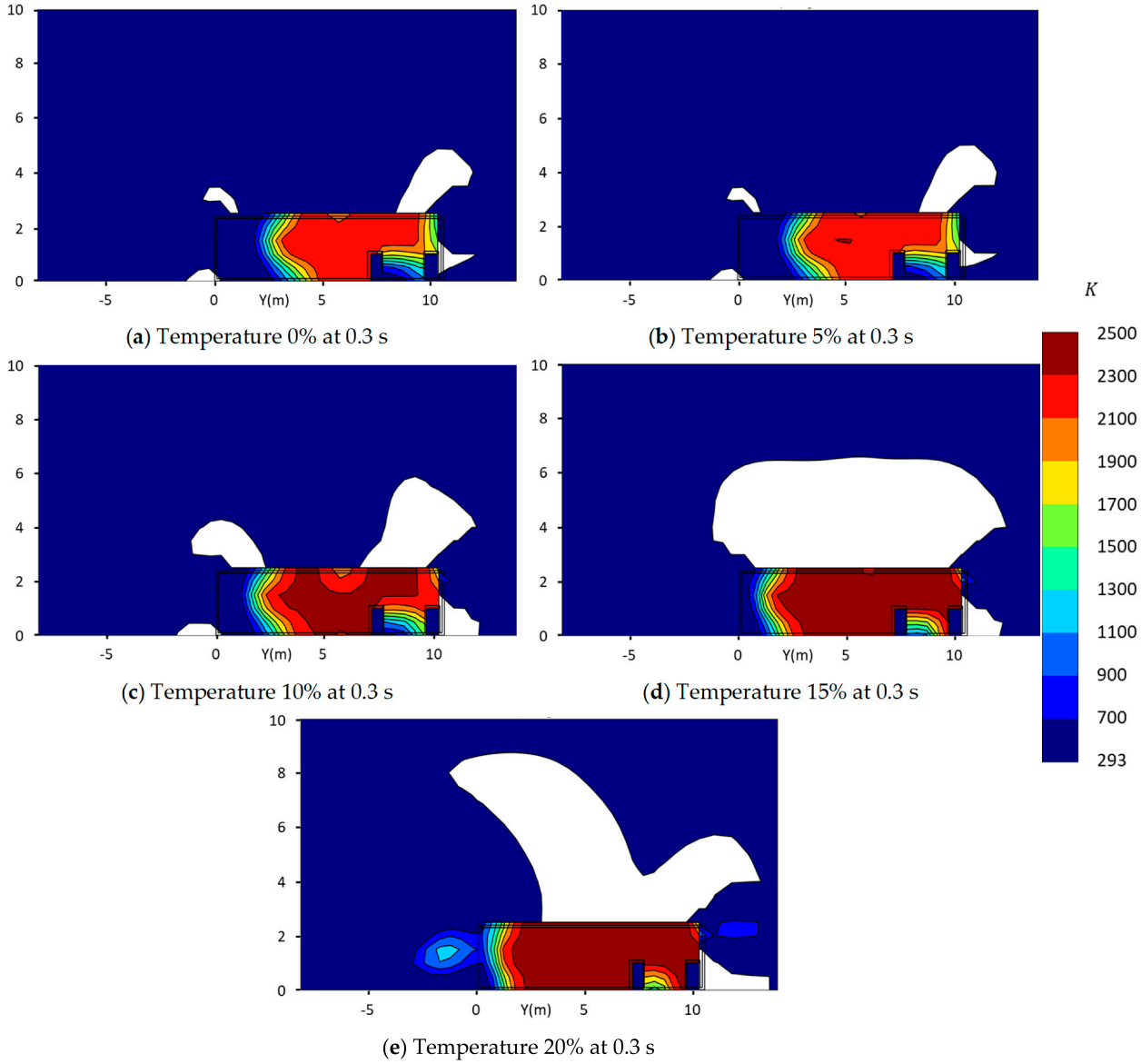

Figure 8. Spatial temperature distributions on the Y–Z plane at X ≈ 3.5 m at approximately 0.3 s for HBRs of (**a**) 0, (**b**) 5, (**c**) 10, (**d**) 15, and (**e**) 20 vol%. A common temperature range of 293–2500 K was applied to all panels.

The maximum temperatures at the common near-source monitoring point were 2374.7, 2387.8, 2402.6, 2417.8, and 2434.1 K for HBRs of 0, 5, 10, 15, and 20%, respectively. The maximum temperature for HBR 20% was 59.4 K, or approximately 2.5%, higher than that for HBR 0%. Although the increase in maximum temperature was relatively smaller than that in maximum overpressure, high-temperature regions developed across a broad area of the apartment under all HBR conditions.

4. Discussion

4.1. Dispersion and Conditional Explosion Responses

The prescribed 30 s low-pressure release produced maximum monitored fuel concentrations corresponding to 1.31–1.49% of the HBR-specific LFLs. All 16 monitoring locations remained below the flammable range, and the maxima occurred at 31.10–37.20 s as transport and redistribution continued after source termination. The 30 s release duration was prescribed as a bounded comparison window with reference to the detector performance

criteria described in Section 2.4. The results characterize gas transport during a time-limited release and show that concentration monitoring remains relevant after the source has been stopped.

The concentration response to HBR depended on location. From HBR 0% to 20%, the maximum increased by 71.6% above the source at P11 and by 12.6% at the living room ceiling at P14, but decreased by 16.3% outside the living room window at P5. Previous enclosure studies have also reported nonuniform methane–hydrogen accumulation governed by release and ventilation conditions [15–22]. Here, the comparison extends across the source ceiling, connecting pathways, occupied rooms, and an exterior opening in an accident-informed apartment. The contrasting local responses indicate that a single concentration value is insufficient to describe the spatial response in this configuration and identify locations for concentration measurements in subsequent experiments.

The dispersion and explosion calculations address two distinct conditions: fuel transport during a prescribed release and explosion consequences once a flammable cloud is present. Minimum ignition energy concerns mixtures within their flammable range; the reduction associated with hydrogen addition [8] does not make the low concentrations recorded at P1–P16 flammable. Accordingly, the explosion cases used an independently prescribed uniform cloud at an equivalence ratio of 1.05. This setup permits comparison of HBR-dependent explosion consequences under a common initial cloud condition. It differs from the leakage-generated cloud approach used by Pang et al. and Lv et al. [21,22].

For the prescribed explosion cloud, increasing HBR from 0% to 20% raised the domain-wide maximum overpressure by 42.9% and the maximum monitored pressure impulse by 21.3%. Peak pressure represents the highest instantaneous loading, whereas impulse includes the duration of loading; the different relative increases, examined quantitatively in Section 4.2.3, support retaining both metrics in consequence assessment. The spatial results additionally showed higher PressureMax regions within connected indoor compartments and lower pressure ranges outside the openings. Together with the enclosure-dependent responses reported in previous residential and vented-explosion studies [20–25], these results motivate closer examination of compartment connections and external openings when evaluating residential hydrogen blending.

4.2. Analytical Consistency Checks and Comparison with Published Data

A formal grid-independence study, an initial-turbulence sensitivity analysis, and a case-specific experimental validation could not be performed in the present study. To make the basis of the reported results transparent, this section (i) compares the released fuel inventory with the amount required for an apartment-scale flammable mixture, (ii) compares the quantities that govern each analysis stage with published experimental data, and (iii) states the basis of each reported conclusion. These analyses provide additional physical context for interpreting the computed results. They do not quantify the discretization uncertainty or the sensitivity to the prescribed initial turbulence.

4.2.1. Inventory Comparison for the Release Stage

The total fuel inventory released during the 30 s release period was calculated from the mass flow rates in Table 4 and the mixture densities at 293.15 K and 101,325 Pa (Table 11). The inventory is 62.2–68.5 L. Distributed uniformly in the nominal apartment volume of 228.8 m^3, this inventory corresponds to 0.027–0.030 vol%, so that an apartment-scale flammable mixture would require approximately 160–180 times the fuel released during the prescribed period. This inventory-based calculation indicates that the released fuel was insufficient to produce a uniformly flammable mixture throughout the nominal apartment volume, and it provides a reference for interpreting the low concentrations predicted at

the monitoring locations. It concerns the released inventory only: it does not address local concentration gradients, the resolution of the near-source region, or the numerical uncertainty of the computed fields. The nominal volume also neglects internal partitions and furnishings, so the actual free volume is somewhat smaller.

Table 11. Released inventory and uniform-mixing reference concentrations.

HBR (Vol%)	Mixture Density (kg/m^3)	Volumetric Release Rate (L/s)	Inventory Released in 30 s (L)	Volume-Averaged Conc. (Vol%) [a]	Maximum Monitored Conc. (Vol%)	Ratio of Maximum to Average
0	0.667	2.07	62.2	0.0272	0.0658	2.42
5	0.638	2.12	63.6	0.0278	0.0678	2.44
10	0.609	2.17	65.1	0.0285	0.0689	2.42
15	0.579	2.22	66.7	0.0292	0.0703	2.41
20	0.550	2.28	68.5	0.0299	0.0711	2.38

[a] Total 30 s inventory distributed uniformly in the nominal apartment volume of 228.8 m^3, without outflow through the openings.

The maximum monitored concentration predicted by FLACS-CFD was 2.38–2.44 times the volume-averaged value for every HBR. The similar ratios across the HBR cases are consistent with the increase in released fuel volume (10.0% from HBR 0% to 20%) contributing to the 8.2% increase in the maximum monitored concentration.

The calculated concentrations at the 16 monitoring locations remained below a hypothetical alarm threshold of 25% of the mixture-specific LFL throughout the simulated period [38]. Under the different assumption of a continuous release with uniform mixing and no air exchange, the corresponding volume-averaged concentration would require tens of minutes to approach that threshold; this is a reference estimate for a different scenario and is not a detector activation time. The prescribed 30 s release duration was used as a bounded comparison window and was not calculated from detector activation.

4.2.2. Release Source and Jet Characteristics

The release source was compared with the domestic-pressure CH_4–H_2 release experiments of Lowesmith et al. [15], who reported release rates of 22.2, 23.2, and 24.5 m^3/h for CH_4, 90:10, and 80:20 CH_4–H_2 mixtures released through a 10 mm hole at a nominal pressure of 30 mbar, corresponding to ratios of 1.000, 1.045, and 1.104, respectively. The FLACS Leak Wizard values in the present study give ratios of 1.000, 1.046, and 1.100 at HBRs of 0, 10, and 20%, respectively (Table 12). When the methane release rate of Lowesmith et al. is scaled to the present opening diameter and supply pressure ($Q \propto d^2P^{0.5}$), it corresponds to 2.02 L/s, compared with 2.07 L/s calculated here, a difference of approximately 3%.

The jet parameters in Table 12 explain the dispersion trends reported in Section 3.2. At a fixed supply pressure, the jet momentum flux, evaluated as the product of the mass flow rate and the release velocity reported in Table 4, varies by less than 0.5% among the HBR cases, whereas the buoyancy flux increases by 34% from HBR 0% to 20% because the mixture density decreases. The densimetric Froude numbers of 357–395 and the momentum length scale of approximately 2.9 m indicate that the near-source transport during injection is governed by the jet, with buoyancy becoming relatively more important at distances comparable to the kitchen dimensions. This combination accounts for the similar overall transport pattern among the HBR cases (Figure 3), for the increase in concentration above the source (P11), where the lighter mixture rises more strongly once the jet momentum has decayed, and for the decrease at the exterior point P5, which is reached mainly by horizontal transport along the jet direction. Lowesmith et al. [15] similarly concluded that hydrogen

addition increases the volumetric release rate and the accumulated concentration, but that the increase is moderated by enhanced buoyancy-driven ventilation.

Table 12. Jet characteristics of the release source and comparison of release rate ratios with published data.

HBR (Vol%)	Release Velocity (m/s)	Momentum Flux (N) [a]	Buoyancy Flux ($\times 10^{-3}$ m^4/s^3)	Densimetric Froude Number	Momentum Length Scale (m)	Distance to LFL on Jet Axis (m) [a]	Release Rate Ratio, Present Study	Release Rate Ratio, Ref. [15] [b]
0	86.08	0.1191	9.07	395	2.88	0.79	1.000	1.00
5	87.74	0.1186	9.78	384	2.86	0.82	1.022	-
10	89.82	0.1187	10.53	374	2.86	0.85	1.046	1.045
15	92.05	0.1187	11.32	365	2.86	0.88	1.072	-
20	94.45	0.1186	12.16	357	2.87	0.91	1.100	1.104

[a] Momentum flux evaluated as the product of the mass flow rate and release velocity in Table 4, and buoyancy flux as g' times the volumetric release rate. Free-jet centerline decay, $c = 5d(\rho j/\rho a)0.5/x$, applied to the fuel mass fraction [43]. [b] 10 mm hole, nominal pressure 30 mbar; ratios of the reported release rates of 22.2, 23.2, and 24.5 m^3/h.

A free-jet centerline decay relation [43] was used to obtain a reference estimate of near-source dilution, which places the LFL at approximately 0.8–0.9 m from the opening (Table 12). Its application to the present configuration is approximate, because the apartment geometry introduces confinement and possible jet–surface interactions. Independently of this estimate, the equivalent stoichiometric cloud volume (Q9), which is evaluated by the solver over the whole domain, remained zero throughout the dispersion simulations (Section 3.1).

4.2.3. Explosion Stage: Scaling Analysis and Comparison with Published Data

To examine whether the predicted HBR dependence is physically consistent, the FLACS-CFD results were compared with simple scaling relations for vented deflagrations. The peak overpressure scales approximately with $[SL(E-1)]^2$ [44], the time to peak pressure with $1/(S_L E)$, and the pressure impulse, approximated as the product of pressure and loading duration, with S_L. Laminar burning velocities were taken from the correlation of Hu et al. [45] for CH_4–H_2–air mixtures at 0.1 MPa, 303 K, and $\varphi = 1.0$, giving $S_{L,20}/S_{L,0} = 1.184$; the directly calculated values in the same study (0.406 and 0.463 m/s) give 1.140. Because the adiabatic flame temperature changes by only 0.3% over this range (2230–2236 K) [45], the expansion ratio varies by less than 1% and was treated as constant. As shown in Table 13, and using the linear burning velocity correlation, the tabulated ratios differed from the scaling estimates by approximately 2% or less for the maximum overpressure, 2.5% or less for the pressure impulse, and 4.3% or less for the time to peak pressure. Using the alternative directly calculated burning velocities at HBR 20% increased the differences to approximately 9.9% for the maximum overpressure and 6.4% for the pressure impulse. The comparison therefore depends on the burning velocity values adopted. The scaling relations also provide a physical interpretation of why the relative increase in maximum overpressure (42.9%) exceeds that in pressure impulse (21.3%): impulse reflects the product of pressure and loading duration, and the duration decreases as S_L increases. Because FLACS-CFD it-self uses mixture-dependent burning velocity inputs, this comparison is presented as a consistency check of the predicted HBR dependence rather than as independent validation.

Table 13. Scaling estimates and FLACS-CFD predictions for the explosion stage, expressed as ratios to HBR 0%.

HBR (Vol%)	S_L (m/s) [a]	S_L Ratio	P_{max}: Scaling (S_L Ratio^2)	P_{max}: FLACS	t_{peak}: Scaling ($1/S_L$ Ratio)	t_{peak}: FLACS	Impulse: Scaling (S_L Ratio)	Impulse: FLACS
0	0.398	1.000	1.000	1.000	1.000	1.000	1.000	1.000
5	0.417	1.046	1.094	1.086	0.956	0.997	1.046	1.046
10	0.435	1.092	1.193	1.196	0.916	0.955	1.092	1.104
15	0.453	1.138	1.295	1.310	0.879	0.910	1.138	1.159
20	0.472	1.184	1.402	1.429	0.844	0.873	1.184	1.213
20 [b]	0.463	1.140	1.300	1.429	0.877	0.873	1.140	1.213

[a] Linear correlation of Hu et al. [45] for 0–40% H_2 (0.1 MPa, 303 K, $\varphi = 1.0$). [b] Directly calculated values of Hu et al. [45] (0.406 and 0.463 m/s).

An energy comparison supports this interpretation. Using standard lower heating values of 802.7 kJ/mol for CH_4 and 241.8 kJ/mol for H_2, derived from the standard enthalpies of combustion and formation [46], the fuel energy release rate of the prescribed leak decreased from 69.2 kW at HBR 0% to 65.5 kW at HBR 20% (−5.3%), although the volumetric release rate increased by 10%. For the prescribed explosion cloud at $\varphi = 1.05$, the combustion energy per unit volume of fuel–air mixture was nearly independent of HBR (3.31 and 3.30 MJ/m^3 at HBR 0% and 20%, −0.5%). The nearly unchanged fuel energy content is consistent with the pressure increase being associated with changes in combustion rate and pressure development, rather than with an increase in the initial fuel energy inventory.

The predicted HBR effect was further compared with published vented-explosion experiments (Table 14). At 20 vol% H_2, the ratio of maximum overpressure relative to methane was 1.02–1.26 in a 69.3 m^3 empty enclosure at an equivalence ratio of about 1.1 [24] and 1.12–3.18 in a 15 m^3 domestic-scale chamber [25]; the highest value in the latter was associated with an acoustically driven oscillatory pressure peak, which grid-based models such as FLACS-CFD are not designed to resolve. The corresponding NFPA 68 estimates reported by Torrado et al. [25] were 1.43–1.67. The present prediction of 1.43 was higher than the 1.02–1.26 range reported for the large-scale enclosure [24], lay within the broader range reported for the domestic-scale chamber [25], and coincided with the lower bound of the NFPA 68 estimates. These comparisons illustrate the dependence of the hydrogen effect on enclosure and experimental conditions. The predicted 12.7% reduction in the time to peak pressure is reported as a computed result and is not compared with the measured flame speeds, which are a different quantity.

Table 14. Published experimental and standard-based ratios of maximum overpressure for 20 vol% H_2 relative to methane.

Source	Configuration	P_{max} Ratio (20% H_2/CH_4)	Flame Speed Ratio
Lowesmith et al. [24]	69.3 m^3 enclosure, empty, ER ≈ 1.1, central/rear ignition	1.02/1.26	1.21/1.08
Torrado et al. [25]	15 m^3 chamber, empty, ER = 0.8/1.0/1.18	1.31/3.18 [a]/1.12	1.12–1.59
NFPA 68:2013, as calculated in [25]	Same conditions as [25]	1.43/1.67/1.60	-
Present study (FLACS-CFD)	Apartment, uniform cloud, $\varphi = 1.05$	1.43	-

[a] Oscillatory peak associated with acoustic–flame interaction.

4.2.4. Basis of the Reported Conclusions and Numerical Uncertainty

The analyses above differ in the type of evidence they provide. First, the fuel released during the prescribed 30 s period was far below the amount required for an apartment-scale flammable mixture, as shown by the inventory comparison in Section 4.2.1. Second, the predicted HBR trends—the increase in maximum monitored concentration, the redistribution towards upper regions near the source, the increase in overpressure and impulse, and the reduction in time to peak pressure—can be compared with the release rate data of Lowesmith et al. [15], with burning velocity scaling, and with published vented-explosion experiments. All explosion cases used an identical grid, geometry, and porosity field, and the dispersion grids differed only in the refined region around the source, so that the prescribed fuel composition was the only variable between the cases; no assumption is made here about how the grid-related error is distributed among them.

Third, the absolute values—local concentrations at distant monitoring points, the overpressures of 0.872–1.246 barg, and the pressure impulses—depend on numerical and modelling assumptions that are not quantified here. The explosion grid has a cell size of approximately 0.5 m (Section 2.2.4), so features of the order of the internal openings are represented through the PDR porosity formulation rather than resolved directly. The rigid wall assumption and the apartment-wide uniform near-stoichiometric cloud both tend to increase the calculated overpressure relative to a partially filled apartment with failing openings. The prescribed initial turbulence corresponds to a velocity fluctuation of approximately 0.05 m/s, about three orders of magnitude below the release velocity; this scale comparison alone does not quantify the sensitivity of the post-release concentrations or of the explosion loading to that field. The absolute values reported here should therefore be interpreted as scenario- and model-specific estimates, and the relative HBR comparisons as the principal outcome of the explosion analysis. These considerations also indicate which quantities a subsequent grid-convergence study should target first, namely the peak overpressure and the near-opening pressure field.

4.3. Implications and Limitations

The principal contribution is the joint examination of release duration, location-dependent gas transport, and conditional explosion loading in an accident-informed multi-compartment apartment. Compared with kitchen-focused analyses, the present model includes pathways through which fuel and pressure can affect adjacent residential spaces. The results provide candidate locations and quantities for future measurements, particularly above the source, along upper connecting paths, and near external openings. For prospective residential hydrogen blending, gas detection, source isolation, ventilation, and user response should be considered together with the apartment layout. The calculated spatial patterns can inform the design of studies addressing these measures and, subsequently, the evidence needed for safety guidance and resident education.

The results also provide data-based input for detector provisions, which have not yet been established for hydrogen-blended gas in general residential rooms (Section 2.4). First, for the prescribed release, the volume-averaged concentration reached only 2.2–2.5% of the 25%–LFL alarm threshold within 30 s, and the maximum monitored concentration reached 5.3–6.0% of that threshold (Section 4.2.1). At the 16 monitoring locations, a concentration-based alarm set at 25% of the mixture-specific LFL would therefore not have been reached during the simulated period. Second, the highest monitored concentrations occurred along the jet path at the kitchen–living room connection (P12) and at the living room ceiling (P14), whereas the point above the source (P11) recorded approximately one-third to one-half of these values. Third, hydrogen addition increased the concentration above the source (P11, +71.6%) and at the living room ceiling (P14, +12.6%) but decreased it outside the window

(P5, −16.3%). The spatial differences in monitored concentration suggest that detector placement should be evaluated together with the release direction, the upper connecting pathways, and the mixture-specific alarm threshold, rather than by reference to the position directly above a potential source alone.

This study is a scenario-based numerical investigation of binary CH_4–H_2 mixtures at HBRs of 0–20 vol% in one apartment configuration with all openings open. The considerations regarding numerical uncertainty are summarized in Section 4.2.4. Future work should extend the assessment to other supplied gas compositions, closed or partially closed ventilation arrangements, longer release durations, and different ambient conditions, for which pressure-dependent combustion behavior has been reported [47,48], and should include grid convergence analysis and apartment-scale experiments representing connected residential compartments.

5. Conclusions

The FLACS-CFD calculations compared low-pressure hydrogen–methane dispersion and independently prescribed explosions in an accident-informed multi-compartment apartment. For the 30 s release, the maximum computed concentration among 16 monitoring points corresponded to 1.31–1.49% of the HBR-specific LFLs. From HBR 0% to 20%, this maximum increased by approximately 8.2%, whereas the local maxima increased by 71.6% at P11 above the source and decreased by 16.3% at exterior point P5. The calculations therefore showed location-dependent concentration responses across the connected apartment.

Under the prescribed near-stoichiometric explosion condition, the calculated domain-wide maximum overpressure increased from 0.872 to 1.246 barg (42.9%), and maximum monitored pressure impulse increased by 21.3%. The ignition-to-peak-pressure interval decreased by 12.7%, while maximum near-source temperature increased by approximately 2.5%. Within the investigated cases, hydrogen addition produced a larger and more rapid pressure response, with different relative changes in peak pressure, impulse, and temperature. The combustion energy per unit volume of the prescribed cloud was nearly independent of HBR, so the increase is consistent with changes in combustion rate and pressure development rather than with a larger fuel energy inventory. The calculated ratios were compared with laminar burning velocity scaling, with differences that depend on the burning velocity values adopted, and lay within the range reported in published vented-explosion experiments.

This study provides a spatially resolved numerical comparison to guide subsequent investigations of hydrogen–methane use in residential apartments. The source ceiling, upper inter-compartment pathways, and exterior opening emerged as useful locations for examining fuel transport, while pressure and impulse provide complementary loading measures. Together, these results support further investigation of gas detection, source isolation, and ventilation in relation to residential layout. At the sixteen monitoring locations, the calculated concentrations remained below 25% of the mixture-specific LFL during the simulated period, indicating that detector placement and alarm thresholds for hydrogen-blended residential gas should be evaluated together with the expected leak rate, the release direction, and the upper connecting pathways. Grid convergence analysis and apartment-scale experiments remain necessary to quantify the absolute values before these findings are translated into practical safety guidance.

Author Contributions: Conceptualization, S.-S.T. and M.J.L.; methodology, S.-S.T. and M.J.L.; software, S.Y.L. and M.S.K.; formal analysis, S.Y.L., M.S.K. and M.J.L.; investigation, S.-S.T.; data curation, M.J.L.; writing—original draft preparation, S.-S.T. and M.J.L.; writing—review and editing, S.-S.T., M.J.L. and J.-B.B.; visualization, S.Y.L. and M.S.K.; supervision, S.-S.T.; project administration, S.-S.T.; funding acquisition, S.-S.T. All authors have read and agreed to the published version of the manuscript.

Funding: This research was funded by the Ministry of Trade, Industry and Energy (MOTIE) of the Republic of Korea through the Korea Institute of Energy Technology Evaluation and Planning (KETEP), grant number RS-2023-00236237. The APC was funded by the same grant.

Data Availability Statement: The data supporting the findings of this study are presented within the article. Additional data, including the raw FLACS-CFD input and output files, are available from the first author upon reasonable request.

Acknowledgments: During the preparation of this manuscript/study, the authors used ChatGPT (OpenAI; models used included 5.6-sol) to assist with Korean–English translation, English language editing, and drafting responses to reviewers. The authors have reviewed and edited the output and take full responsibility for the content of this publication.

Conflicts of Interest: The authors declare no conflicts of interest.

References

1. International Energy Agency. *The Future of Hydrogen: Seizing Today's Opportunities*; International Energy Agency: Paris, France, 2019. Available online: https://www.iea.org/reports/the-future-of-hydrogen (accessed on 25 July 2026).
2. Mahajan, D.; Tan, K.; Venkatesh, T.; Kileti, P.; Clayton, C.R. Hydrogen blending in gas pipeline networks—A review. *Energies* **2022**, *15*, 3582. [CrossRef]
3. Melaina, M.W.; Antonia, O.; Penev, M. *Blending Hydrogen into Natural Gas Pipeline Networks: A Review of Key Issues*; NREL/TP-5600-51995; National Renewable Energy Laboratory: Golden, CO, USA, 2013. [CrossRef]
4. Isaac, T. HyDeploy: The UK's first hydrogen blending deployment project. *Clean Energy* **2019**, *3*, 114–125. [CrossRef]
5. Ministry of Trade, Industry and Energy. Research Begins on Hydrogen Blending into City Gas. 16 May 2023. Available online: https://www.motir.go.kr/kor/article/ATCL3f49a5a8c/167214/view (accessed on 22 September 2026). (In Korean)
6. Australian Gas Infrastructure Group. Hydrogen Park South Australia. Available online: https://www.agig.com.au/hydrogen-park-south-australia (accessed on 22 September 2026).
7. Molnarne, M.; Schroeder, V. Hazardous properties of hydrogen and hydrogen-containing fuel gases. *Process Saf. Environ. Prot.* **2019**, *130*, 1–5. [CrossRef]
8. Hankinson, G.; Mathurkar, H.; Lowesmith, B.J. Ignition energy and ignition probability of methane–hydrogen–air mixtures. In Proceedings of the 3rd International Conference on Hydrogen Safety, Ajaccio, France, 16–18 September 2009; Paper 125.
9. Zhou, C.; Yang, Z.; Chen, G.; Zhang, Q.; Yang, Y. Study on leakage and explosion consequence for hydrogen-blended natural gas in urban distribution networks. *Int. J. Hydrogen Energy* **2022**, *47*, 27096–27115. [CrossRef]
10. Li, H.; Cao, X.; Du, H.; Teng, L.; Shao, Y.; Bian, J. Numerical simulation of leakage and diffusion distribution of natural gas and hydrogen mixtures in a closed container. *Int. J. Hydrogen Energy* **2022**, *47*, 35928–35939. [CrossRef]
11. Yang, K.; Li, W.; Dai, X.; Guo, Y.; Pang, L. Effect of hydrogen ratio on leakage and explosion characteristics of hydrogen-blended natural gas in utility tunnels. *Int. J. Hydrogen Energy* **2024**, *64*, 132–147. [CrossRef]
12. Liu, E.; Li, T.; Pang, J. Research on the leakage characteristics of hydrogen-blended natural gas pipelines in urban residential courtyards. *Int. J. Hydrogen Energy* **2025**, *189*, 152178. [CrossRef]
13. Qin, J.; Xie, Y.; Liu, J.; Xu, Z.; Meng, S.; Zhu, J.; Liu, G.; Yuan, H. Research on leakage and diffusion of hydrogen-blended natural gas in a ship engine room. *Int. J. Hydrogen Energy* **2025**, *160*, 150537. [CrossRef]
14. Wang, K.; Li, C.; Jia, W.; Chen, Y.; Wang, J. Study on multicomponent leakage and diffusion characteristics of hydrogen-blended natural gas in utility tunnels. *Int. J. Hydrogen Energy* **2024**, *50*, 740–760. [CrossRef]
15. Lowesmith, B.J.; Hankinson, G.; Spataru, C.; Stobbart, M. Gas build-up in a domestic property following releases of methane/hydrogen mixtures. *Int. J. Hydrogen Energy* **2009**, *34*, 5932–5939. [CrossRef]
16. Marangon, A.; Carcassi, M.N. Hydrogen–methane mixtures: Dispersion and stratification studies. *Int. J. Hydrogen Energy* **2014**, *39*, 6160–6168. [CrossRef]
17. Su, Y.; Li, J.; Yu, B.; Zhao, Y. Numerical investigation on the leakage and diffusion characteristics of hydrogen-blended natural gas in a domestic kitchen. *Renew. Energy* **2022**, *189*, 899–916. [CrossRef]
18. Li, M.; Chen, S.; Jiang, W.; Li, Y.; Xu, Z.; Guan, B.; Wang, X.; Lin, X.; Liu, T. Numerical simulation analysis of the hydrogen-blended natural gas leakage and ventilation processes in a domestic house. *ACS Omega* **2023**, *8*, 34610–34628. [CrossRef] [PubMed]
19. Thawani, B.; Hazael, R.; Critchley, R. Numerical modelling of hydrogen leakages in confined spaces for domestic applications. *Int. J. Hydrogen Energy* **2024**, *56*, 797–806. [CrossRef]

20. Xu, H.; Deng, Q.; Huang, X.; Li, D.; Pan, F. Simulation and experimental verification of dispersion and explosion of hydrogen–methane mixture in a domestic kitchen. *Energies* **2024**, *17*, 2320. [CrossRef]
21. Pang, L.; Wang, Z.; Wang, Y.; Zheng, J.; Zhao, H.; He, N. Explosion venting of indoor hydrogen-blended natural gas: Distribution law of compound hazards driven by "leakage–accumulation" effect. *Int. J. Hydrogen Energy* **2025**, *101*, 379–390. [CrossRef]
22. Lv, P.; Zhang, J.; Shen, J.; Yang, K. Effect of hydrogen-blended ratio on the leakage and explosion characteristics of hydrogen-blended natural gas in residential kitchens. *Fuel* **2026**, *409*, 137883. [CrossRef]
23. Peng, S.; Zhou, W.; Luo, X.; Liu, E. Analysis of the consequences of hydrogen-blended natural gas explosions in a residential building. *Int. J. Hydrogen Energy* **2024**, *95*, 463–480. [CrossRef]
24. Lowesmith, B.J.; Mumby, C.; Hankinson, G.; Puttock, J.S. Vented confined explosions involving methane/hydrogen mixtures. *Int. J. Hydrogen Energy* **2011**, *36*, 2337–2343. [CrossRef]
25. Torrado, D.; Fletcher, J.; Sanderson, E.; Tooke, A.; Hooker, P.; Isaac, T.; Manson-Whitton, C.; Lander, D.; Spriggs, C. Experimental study of the explosion severity of vented methane/hydrogen deflagrations. In Proceedings of the International Conference on Hydrogen Safety, Edinburgh, UK, 21–23 September 2021. Available online: https://hysafe.info/uploads/papers/2021/22.pdf (accessed on 25 July 2026).
26. Yang, K.; Wu, H.; Chen, Y. Effect of room layout on natural gas explosion in kitchen. *Fire* **2024**, *7*, 235. [CrossRef]
27. Yang, H.; Qi, S.; Hu, Q.; Wang, J.; Qian, X.; Yuan, M.; Li, P. Natural gas explosion characteristics and structural failures in typical residence under different ignition positions. *Energy* **2025**, *336*, 138603. [CrossRef]
28. Deng, X. A new open-source library based on novel high-resolution structure-preserving convection schemes. *J. Comput. Sci.* **2023**, *74*, 102150. [CrossRef]
29. Tak, S.-S.; Lim, K.-S. Analysis of indoor gas leakage amounts by hydrogen blending ratio using city gas accident cases. *Ind. Promot. Res.* **2025**, *10*, 163–170. [CrossRef]
30. Korea Gas Safety Corporation. *Gas Accident Almanac 2023*; Korea Gas Safety Corporation: Eumseong, Republic of Korea, 2024; pp. 28–29.
31. Statistics Korea. *Results of the 2023 Population and Housing Census*; Statistics Korea: Daejeon, Republic of Korea, 2024; pp. 46–48, 60–61.
32. Gexcon AS. *FLACS-CFD*, Version 25.2; Gexcon AS: Bergen, Norway, 2025. Available online: https://www.gexcon.com/software/flacs/ (accessed on 22 September 2026).
33. Middha, P.; Hansen, O.R.; Grune, J.; Kotchourko, A. CFD calculations of gas leak dispersion and subsequent gas explosions: Validation against ignited impinging hydrogen jet experiments. *J. Hazard. Mater.* **2010**, *179*, 84–94. [CrossRef] [PubMed]
34. Hansen, O.R.; Renoult, J.; Sherman, M.P.; Tieszen, S.R. Validation of FLACS-Hydrogen CFD consequence prediction model against large-scale H_2 explosion experiments in the FLAME facility. In Proceedings of the 1st International Conference on Hydrogen Safety, Pisa, Italy, 8–10 September 2005.
35. Hjertager, B.H. Simulation of transient compressible turbulent reactive flows. *Combust. Sci. Technol.* **1982**, *27*, 159–170. [CrossRef]
36. Hjertager, B.H. Influence of turbulence on gas explosions. *J. Hazard. Mater.* **1984**, *9*, 315–346. [CrossRef]
37. Gexcon AS. *FLACS-CFD v25.2 User's Manual*; Gexcon AS: Bergen, Norway, 2025. Available online: https://www3.gexcon.com/files/packages/flacs-users-manual-25.2.pdf (accessed on 1 November 2025).
38. Korea Gas Safety Corporation. *Facility/Technical/Inspection Code for Urban Gas Using Facilities*; KGS FU551 2026; Korea Gas Safety Corporation: Eumseong, Republic of Korea, 2026.
39. Gexcon AS. Setting a Leak. FLACS-CFD Knowledge Base. 2024. Available online: https://knowledge.gexcon.com/docs/setting-a-leak (accessed on 1 August 2026).
40. Korea Gas Safety Corporation. *Facility/Technical/Inspection Code for Use of Specified High-Pressure Gases*; KGS FU211 2026; Korea Gas Safety Corporation: Eumseong, Republic of Korea, 2026.
41. Korea Occupational Safety and Health Agency. *Technical Guideline for Installation and Maintenance of Gas Leak Detection and Alarm Systems*; KOSHA Guide P-166-2020; Korea Occupational Safety and Health Agency: Ulsan, Republic of Korea, 2020.
42. Gexcon AS. Boundary Conditions. FLACS-CFD Knowledge Base. 2024. Available online: https://knowledge.gexcon.com/docs/boundary-conditions (accessed on 1 August 2026).
43. Chen, C.J.; Rodi, W. *Vertical Turbulent Buoyant Jets: A Review of Experimental Data*; Pergamon Press: Oxford, UK, 1980.
44. National Fire Protection Association. *NFPA 68: Standard on Explosion Protection by Deflagration Venting, 2013*; NFPA: Quincy, MA, USA, 2013.
45. Hu, E.; Huang, Z.; Zheng, J.; Li, Q.; He, J. Numerical study on laminar burning velocity and NO formation of premixed methane–hydrogen–air flames. *Int. J. Hydrogen Energy* **2009**, *34*, 6545–6557. [CrossRef]
46. Linstrom, P.J.; Mallard, W.G. (Eds.) *NIST Chemistry WebBook, NIST Standard Reference Database Number 69*; National Institute of Standards and Technology: Gaithersburg, MD, USA, 2025. [CrossRef]

47. Qi, S.; Yang, Z.; Li, Y.; Jing, Q.; Zhang, L. Flame propagation, explosion hazard, and pollutant emission characterization of typical clean fuels leaks in plateau low-pressure region. *Fuel* **2025**, *379*, 133121. [CrossRef]
48. Al-Khafaji, M.; Yang, J.; Tomlin, A.S.; Thompson, H.M.; de Boer, G.; Liu, K.; Morsy, M.E. Laminar burning velocities and Markstein numbers for pure hydrogen and methane/hydrogen/air mixtures at elevated pressures. *Fuel* **2023**, *354*, 129331. [CrossRef]

Disclaimer/Publisher's Note: The statements, opinions and data contained in all publications are solely those of the individual author(s) and contributor(s) and not of MDPI and/or the editor(s). MDPI and/or the editor(s) disclaim responsibility for any injury to people or property resulting from any ideas, methods, instructions or products referred to in the content.